Journal of Applied Fluid Mechanics, Vol. 17, No. 2, pp. 352-369, 2024.
Available online at www.jafmonline.net, ISSN 1735-3572, EISSN 1735-3645.
https://doi.org/10.47176/jafm.17.02.2118

Exploring the Diagnostic Potential of Infrared Thermography for Experimental Assessment of Cavitation and Air Entrainment-induced Faults in Centrifugal Pumps

A. K. Goel† and V. N. A. Naikan

SCSQR, Indian Institute of Technology (IIT), Kharagpur, West Bengal, 721302, India

†*Corresponding Author Email: anujkumargoel@kgpian.iitkgp.ac.in*

ABSTRACT

This research pioneers the application of thermographic principles to diagnose faults, specifically cavitation and air entrainment, in centrifugal pumps. The study represents the inaugural investigation into the feasibility of leveraging infrared thermography for this purpose, underpinned by rigorous experimental methodologies to validate its efficacy. By capturing thermal images of pumps operating under varying conditions, a pseudo-coloring technique for precise temperature range segmentation was employed. This technique facilitated the assessment of fault severity, quantified through the computation of the $Thermal_{index}$. This index emerged as a quantifiable metric of fault severity, with elevated values correlating to more pronounced degrees of fault occurrence. Notably, in the case of air entrainment faults, a maximum temperature escalation of 3.9°C was recorded after 60 min run time, and the corresponding thermal index was found to be 5.12. The investigation employs the HSV model, extracting regions of thermal variation through hue differences for fault detection. This process is combined with edge detection methods like Sobel, Prewitt, Roberts, Canny, and Otsu. The Otsu technique consistently outperformed alternative approaches. Specifically, for high cavitation and air entrainment faults, the Otsu method had the highest mean of 0.1730 and 0.1253, respectively. Key findings include the effectiveness of image processing techniques, statistical measures, and edge detection methods for fault diagnosis, as well as insights into temperature differentials and motor load reductions with increasing fault severity. The research improves maintenance, enhancing efficiency and reducing downtime. It emphasizes infrared thermography's potential for fault diagnosis while identifying constraints and advocating further research.

Article History

Received June 21, 2023
Revised September 13, 2023
Accepted October 5, 2023
Available online December 4, 2023

Keywords:

Condition monitoring
Rotating machinery
Fault diagnosis
Image processing
Thermal imaging

1. INTRODUCTION

Hydraulic devices known as pumps are frequently employed in various industrial applications to effectively transport fluids from one location to another. Centrifugal pumps are of particular importance in water supply systems, chemical plants, power plants, and the gas and oil sector for fluid transport, as reported in (Stan et al., 2018; Kan et al., 2022). These pumps account for approximately 64% of all pump sales in industrially developed countries, as per the ISO 2004 standard as reported in (Kan et al., 2022). Malfunctions of centrifugal pumps can alter their operation, reducing efficiency or leading to complete failure. Such failures may result from hydraulic or mechanical factors. Examples of hydraulic failure include cavitation, axial thrust, radial thrust, and air entrainment, while mechanical failures include lubrication, fatigue, bearing, excessive vibration, and more. The main centrifugal pump failure modes are described in (Mckee et al., 2011).

In critical industrial applications, centrifugal pumps play a significant role in the production line, and their sudden failure can result in direct and indirect losses, such as stopping local production or increasing maintenance costs, as noted in (McKee et al., 2014; Paripurna Kamiel, 2015). It is therefore important to properly monitor, diagnose,

NOMENCLATURE

AE	acoustic Emission	PSNR	Peak to Signal Noise Ratio,
C	canny	ΔP_{inlet}	inlet pressure changes
DAQ	Data Acquisition System	ROI	Region Of Interest
$f(x,y)$	2D image function	R(r,c)	RGB thermal image
$Gradf$	local rate of change in pixel intensity across an image	R	roberts
Gx,y	gaussian function at a given point (x,y) in the image	R_1 ,R_2 ,R_3	range 1, range 2 and range 3
Gx, Gy	mask for the x direction, Mask for the y direction	SD	Standard Deviation
G(r,c)	greyscale image	S	sobel
HSV	Hue-Saturation-Value	T_{max}	maximum temperature
IRT	Infrared thermography	T_a	ambient temperature
LTSA	Load Torque Signature Analysis	VFD	Variable Frequency Drive
MSE	Mean Square Error,	W_{high} , W_{low},	number of pixels in the region R_3 of high and low severity fault greyscale images
MoASoID	Method of Area Selection of Image Differences	∂f/ ∂x and ∂f/ ∂y	partial derivatives of f with respect to x and y
NETA	International Electrical Testing Association	σ	standard deviation of the Gaussian distribution
O	otsu		

repair, and replace these pumps before they fail catastrophically, to minimize downtime, material expenses, and maintenance costs. Air entrainment and internal vapor formation caused by cavitation are known to adversely affect centrifugal pumps which lead to increased noise and vibration throughout the system and decreased pump efficiency, as discussed in (Schäfer et al., 2017; Soni, 2017; Sanchez et al., 2018). The focus of this research work is on identifying and assessing the severity of air entrainment and cavitation failures.

Cavitation refers to the creation of cavities inside a flow in the absence of air injection or heat input, which can result in impeller blade erosion and pitting. This can ultimately cause sudden pump failure caused by a broken impeller or defective parts (e.g., bearing or mechanical seal) as discussed in (Muhirwa et al., 2016). When the fluid includes air bubbles before it is pumped, air entrainment occurs. During operation, the pump may be able to take up and suction these air bubbles as noted in (Liao et al., 2021).

Predictive maintenance using condition monitoring techniques has become increasingly important for detecting centrifugal pump failures. Various non-destructive testing (NDT) techniques have been utilized, such as vibration analysis (McKee et al., 2014; Paripurna Kamiel, 2015; Al-Obaidi & Towsyfyan, 2019), acoustic emission (Alfayez et al., 2005), noise emission (Chudina, 2003; Čudina, 2003), flow visualization (Kazi et al., 2011), and ultrasonic testing (Yan et al., 2015). However, current NDT techniques in literature cannot be efficiently employed in industry for detecting faults in centrifugal pumps, due to some technical constraints. For example, vibration analysis requires an expensive setup, such as sensors and data collecting devices, and takes a lot of time to compute and diagnose the fault. Flow visualization and noise emission require access to the cavitation zone and are only limited to clear fluids (Thobiani & Al Thobiani, 2011). The AE technique suffers from wave distortion, and the background noise mostly affects the AE signal (Towsyfyan et al., 2018).

Several methods have been proposed to detect cavitation in centrifugal pumps, such as load torque signature analysis (LTSA) (Stopa et al., 2014), calculating pump pressure using a nonlinear model and the pump's characteristic curve (Samanipour et al., 2017), and using a capacitive sensor to detect cavitation by measuring the change in amplitude of vapor bubbles (Thobiani & Al Thobiani, 2011). These methods, however, rely on pump and motor characteristics to detect cavitation. A flow visualization approach that combines flow-induced parameters and pressure pulsation measures to detect air entrainment in centrifugal pumps has also been developed (Liao et al., 2021). Nonetheless, these techniques solely depend on fault visualization techniques, which are only applicable to clear fluids. (Sojoudi et al., 2018) chose different pumps to test for elevated temperatures during part-load operation. The collected data show that the higher the impeller's rotational speed, the more quickly the water temperature rises. (Hosien & Selim, 2017) conducted an experimental investigation of the cavitation breakdown in centrifugal pumps with water temperatures ranging from 20 °C to 90 °C. They discovered that the cavitation number for the cavitation breakdown increased with rising temperatures and decreased with the continuous temperature increase. (Al-Obaidi & Mohammed, 2019) uses computational fluid dynamics (CFD) to simulate the transient flow and pressure fluctuations in an axial flow pump under different operating conditions. In (Al-Obaidi, 2019) CFD is used to study the flow field and pressure fluctuations in an axial flow pump, but focuses on the unsteady flow patterns caused by guide vanes. Experiments with air injection as a method to improve the performance and reduce the cavitation of a centrifugal pump. It measures the vibration

signals of the pump under different air injection rates and locations, and evaluates the effect of air injection on the head, power, and efficiency of the pump was done by (Al-Obaidi & Mishra, 2020). (Al-Obaidi, 2020a) compares two techniques for detecting and evaluating cavitation in a centrifugal pump: vibration analysis and acoustic analysis. It tests the pump under various operating conditions and analyzes the vibration and acoustic signals to identify the onset, development, and severity of cavitation. In (Al-Obaidi, 2020c) CFD model to simulate the unsteady flow in an axial pump with guide vanes which investigates the effects of guide vane number, angle, and position on the flow fields, pressure fluctuations, and performance characteristics of the pump. The use of acoustic analysis to study cavitation in a centrifugal pump which measures the acoustic signals of the pump under different flow rates and suction pressures, and analyzes the frequency spectra and sound pressure levels to characterize cavitation was done by (Al-Obaidi, 2020b). (Al-Obaidi, 2021) analyzes how different impeller blade angles affect the performance and pressure fluctuations of an axial pump. It uses time-domain and frequency-domain methods to investigate the relationship between blade angle, flow rate, head, efficiency, and pressure fluctuation intensity. Few of the papers use infrared thermography as a method for detecting or evaluating cavitation or air entrainment. Other techniques such as CFD, vibration, and acoustic analysis are used especially in centrifugal pumps. Few experimental papers consider air entrainment as a factor or a fault in the pump operation.

The phenomena of centrifugal pumps are significantly impacted by temperature. Currently, few attempts have been made to include temperature-related information in the predictive maintenance of centrifugal pumps for cavitation and air entrainment phenomena. To address these issues, the development of infrared thermography (IRT) condition monitoring is needed. This technique involves analyzing the temperature distribution of centrifugal pumps to observe cavitation and air entrainment phenomena. IRT is a non-destructive, safe, and reliable technique that can provide extensive inspection coverage (Goel et al., 2022). (Al-Musawi et al., 2020) used thermal image segmentation to create a novel coloring model and categorize various bearing problems in a three-phase induction motor. A feature extraction technique known as the Method of Area Selection of Image Differences (MoASoID) was proposed by (Glowacz & Glowacz, 2017). This method seeks to detect defects by picking the area with the greatest change and feeding these attributes into the classification algorithm. Similarly, (Glowacz et al., 2015) presented a study on monochrome thermal image analysis for pattern recognition, which utilized the area perimeter vector in detecting faulty rotors in motors, relying on the Bayes classifier. In (Singh et al., 2016b), Utilizing the International Electrical Testing Association (NETA) criteria, based on two thermal profile indicators, the authors proposed a method for recognizing cooling system failures and inter-turn problems. Additionally, (Singh et al., 2016a) investigated the use of infrared thermography for detecting cooling system failures, which is crucial for reducing motor temperature. In (Hidayat et al., 2018), the k-means algorithm is used with a combination of vibration signals and thermal image features, to extract shape features using image segmentation for different bearing faults in centrifugal pumps. Although IRT is widely used in the predictive maintenance of induction motors, it has been underutilized for health monitoring and fault diagnostics of centrifugal pumps. It appears that the health information of the centrifugal pump can be obtained from a thermal picture, which can be processed using a variety of image-processing techniques. Infrared thermography offers significant benefits over conventional methods for fault diagnosis of cavitation and air entrainment issues in centrifugal pumps, including enhanced precision and the capacity to diagnose centrifugal pump faults with simplicity. There is no information in the literature that such cavitation modes cause a significant measurable increase in the fluid temperature or pump body temperature increase. (Hidayat et al., 2018; Al-Musawi et al., 2020) successfully explored the potential of thermal analysis in centrifugal pumps and induction motors for different bearing faults using image segmentation, which further validates the use of IRT in centrifugal pumps and induction motors. It is worth investigating faults other than bearing faults in centrifugal pumps using IRT. These two experimental research work validates the use case of IRT for fault diagnosis of centrifugal pumps.

The research work presents a new approach for condition monitoring and fault diagnosis of centrifugal pumps with a comprehensive methodology for fault detection and fault severity analysis (cavitation and air-entrainment fault), outlined in a flowchart diagram Fig. 1. The first step involves seeding an artificial fault into the centrifugal pump, which is an integral part of the experimental rig. This process allows for the simulation of real-world conditions and facilitates the evaluation of the proposed methodologies. Subsequently, thermal images are captured using a thermal camera, capturing

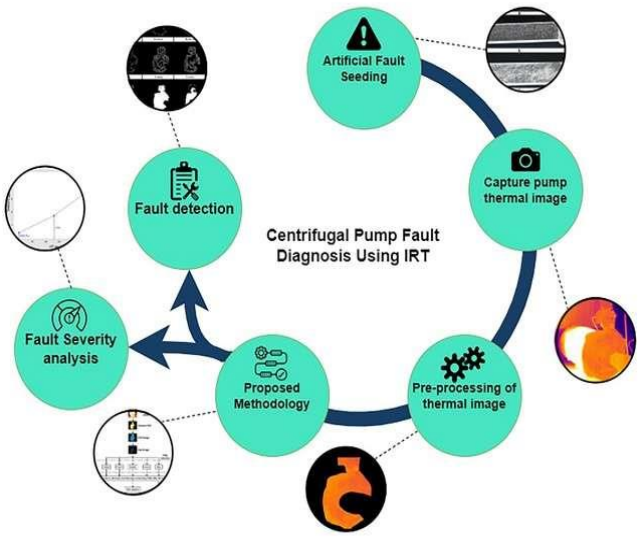

Fig. 1 Proposed methodology for fault diagnosis of the centrifugal pump using IRT

important data for analysis. To prepare the thermal images for further processing, a thermal image pre-processing step is performed. This step includes adjusting the temperature range of the thermal image and cropping the region of interest (ROI) to focus on the relevant areas. Once the pre-processing is complete, the proposed methodologies, as explained in *Sections 3 and 4* of the paper, are applied to the cropped ROI. These methodologies are specifically designed for fault detection and fault severity analysis. By following this systematic approach, the study aims to provide valuable insights and contribute to the field of fault analysis in centrifugal pumps.

The major contributions of this research paper are as follows:

- Demonstrating the effectiveness of infrared thermography for diagnosing faults related to cavitation and air entrainment in centrifugal pumps.
- Highlighting the advantages of using image processing techniques, including a pseudo-color methodology, statistical measures, and edge detection techniques, to analyze thermal images obtained from infrared thermography.
- Proposing a segmentation model based on the Hue color model that can effectively identify cavitation and air entrainment faults in centrifugal pumps without requiring the use of any classifier.
- Shows that image metrics play a crucial role in extracting essential information from the segmented Hue image, enabling accurate recognition of pump faults.
- Addressing difficulties in distinguishing between the severity of faults and proposing further research to improve fault severity estimation.

The major difference in our research work is the new approach for diagnosing faults like cavitation and air entrainment in centrifugal pumps. The application of the pseudo-coloring model and edge detection techniques on IRT images for analyzing different cavitation severities. Proposing a new algorithm for optimizing experimental results and fault severity index. The methodology has not been explored in this area by other authors.

1.1 Thermal Image Processing

In this novel research, the thermal aspects of centrifugal pumps under the effects of cavitation and air entrainment phenomena have been studied. Some emphasis has also been given to the monitoring of pump and motor parameters. Fault diagnosis and severity analysis have been achieved through statistical measures and the latest edge detection techniques.

The research proposes two novel approaches for fault detection and fault severity analysis in centrifugal pumps using thermal images. The first approach employs a pseudo-coloring method to identify different temperature ranges of a thermal image using a color template and compute the fault severity index. In the second approach, the thermal image is converted to the Hue-Saturation-Value (HSV) color model instead of grayscale, to preserve important information. Due to the thermal image's color change from red to green to blue, grayscale approaches may result in information loss. Image segmentation algorithms such as Otsu, Roberts, Sobel, Canny, and Prewitt were used to detect areas of temperature fluctuation.

The image matrices, such as Mean, Kurtosis, Skewness, Contrast, Edge connectivity, PSNR, MSE, SD, and Entropy, were utilized to extract precise fault information from the image. In addition, the areas of thermal variations were detected through the Hue component of the HSV color model, which was found to be especially effective in detecting centrifugal pump faults. After that, it was used for further processing.

The nonlinear transformation of the HSV color model was chosen for processing and evaluating the thermal picture of centrifugal pumps because it is a more exact and effective way for statistical computation and human visual evaluation than the commonly used RGB color model. Using thermal images, we hope to obtain the most reliable defect data for fault diagnosis in centrifugal pumps.

1.2 Image Segmentation

Image segmentation is a crucial procedure in digital image processing that involves dividing an image into multiple segments or regions. There are three primary approaches to image segmentation:

a) The first method includes determining thresholds based on the distribution of pixel attributes, usually applied to image pixel intensity. A digital image is converted into a binary image for subsequent processing using this method.

b) The second strategy comprises using discontinuities in intensity level to identify the borders between all regions. Based on a specific set of rules, such as having all image pixels within a region having the same gray level, the image is divided into sub-regions. It relies on the clustering of neighboring pixels, which are sometimes referred to as regions based on their functional and anatomical roles.

c) The third strategy is edge-based, involving the detection of any quick intensity value deltas, often known as edge detection methods. This methodology is mostly used to detect gray-level discontinuities.

In this study, the edge detection techniques used for thermal image segmentation will be discussed, as the selection of an appropriate image segmentation technique depends on the specific problem which needs to be segmented. Standard edge detection techniques are used with clamp/replicate boundary conditions.

1.3 Edge Detection

Sobel edge detection uses two 3x3 filters to calculate approximate derivatives in the x and y directions, producing smoother results than Roberts but more sensitive to noise than Prewitt. The Sobel filters are defined by the following masks (1) (2) (Al-Musawi et al., 2020):

$$Gx = [-1\ 0\ 1;\ -2\ 0\ 2;\ -1\ 0\ 1] \quad (1)$$

$$Gy = [-1\ -2\ -1;\ 0\ 0\ 0;\ 1\ 2\ 1] \quad (2)$$

Where Gx is the mask for the x direction and Gy is the mask for the y direction with 2D image function $f(x,y)$ and $\partial f/\partial x$ and $\partial f/\partial y$ are the partial derivatives of f with respect to x and y, respectively.

$$Grad(f) = \sqrt{\left(\frac{\partial f}{\partial x}\right)^2 + \left(\frac{\partial f}{\partial y}\right)^2} \quad (3)$$

$Grad(f)$ (3) (Al-Musawi et al., 2020) refers to the approximation of the local rate of change in pixel intensity across an image, calculated using a set of fixed filters for Sobel, Prewitt, and Roberts.

Prewitt edge detection also uses two 3x3 filters to calculate approximate derivatives in the *x* and *y* directions (4) (5) (Al-Musawi et al., 2020), producing fewer sensitive results to noise than Sobel but less smooth results than Roberts.

$$Gx = [-1\ 0\ 1;\ -1\ 0\ 1;\ -1\ 0\ 1] \quad (4)$$

$$Gy = [-1\ -1\ -1;\ 0\ 0\ 0;\ 1\ 1\ 1] \quad (5)$$

Roberts edge detection uses two 2x2 filters to calculate approximate derivatives in the *x* and *y* directions (6) (7) (Al-Musawi et al., 2020), producing the most sensitive results to noise but with the least computational complexity among the above two.

$$Gx = [+1\ 0;\ 0\ -1] \quad (6)$$

$$Gy = [\ 0\ +1;-1\ 0] \quad (7)$$

Canny edge detection uses a multi-stage algorithm involving Gaussian smoothing, gradient magnitude calculation, non-maximum suppression, and hysteresis thresholding to produce high-quality edge maps with minimal noise and thin edges. Gaussian smoothing, which is the noise reduction technique used in Canny edge detection:

$$G(x,y) = \left(\frac{1}{\sqrt{2\pi\sigma^2}}\right) * \exp\left(-\frac{x^2+y^2}{2\sigma^2}\right) \quad (8)$$

Where $G(x,y)$ (8) (Al-Musawi et al., 2020) is the Gaussian function at the point (x,y), σ is the standard deviation of the Gaussian distribution. It is used to calculate the value of the Gaussian function at a given point (x,y) in the image, which is then used to weigh the contribution of neighboring pixels in the smoothing process.

In canny gradient refers to the magnitude and direction of the image gradient calculated using Gaussian smoothing and derivative filters, which is used to identify potential edge locations calculated using (3) (Al-Musawi et al., 2020).

Otsu thresholding is a technique for automatic image thresholding that calculates an optimal threshold value to separate foreground and background pixels based on the image histogram, producing accurate results with minimal user intervention.

To determine the threshold value for image intensity, the image is divided into two regions, and the mean gray-level values for each region are calculated. A new threshold is then selected and the process is repeated until the mean gray-level values for the regions no longer change. The rest of the paper has been organized as follows: Section 2: describes the test rig and experimental procedures, Sections 3 & 4: present the proposed methodologies, Section 5: discusses the obtained results, and Section 6: presents the conclusions drawn from the results.

2. CENTRIFUGAL PUMP EXPERIMENTAL SETUP & PROCEDURES

The experimental setup employed in this study is shown in Fig. 2. The test rig is equipped with a variety of equipment, including (1) Control panel (2) VFD (Variable Frequency Drive) (3) DAQ (Data Acquisition System) (4) Three-phase 0.75 kW induction motor (5) Centrifugal pump-Cast iron (6) Rotameter (7) Discharge valve (8) Pressure gauges (9) Vacuum gauge (10) Inlet valve (11) Water tank (12) Piping (13) Air injection valve (14) Heavy duty tripod (15) Thermal camera (FLIR-E60) (16) Optical tachometer (17) Water temperature meter.

Thermal images of a functioning pump were taken during the experiment to serve as a reference for comparing the faulty images. Two types of fault were investigated in this research which are cavitation and air entrainment. Two levels of fault severity for each type of fault were introduced in the system which is low and high. The fault descriptions are given in Table 1 and Table 2

The inlet pressure of the pump was taken as the reference for describing the fault severity concerning bubble formations since centrifugal pumps do not operate on the same levels when they are reset.

The experimental setup involved inducing the cavitation effect by throttling the inlet valve and introducing air entrainment through a controlled small opening in the inlet pipe.

By associating "low" and "high" fault states with varying valve openings, directly correlated with inlet pressure as observed in Table 1 and Table 2, we explored the impact of these fault states. As

Table 1 Cavitation fault description

Fault Level	Inlet Pressure (inHg)	% Decrease (Ref: Healthy)
Healthy	-13.25	0
Low	-16.75	26
High	-22.25	67

Table 2 Air Entrainment fault description

Fault Level	Inlet Pressure (inHg)	% Increase (Ref: Healthy)
Healthy	-13.25	0
Low	-13	2
High	-11.75	11

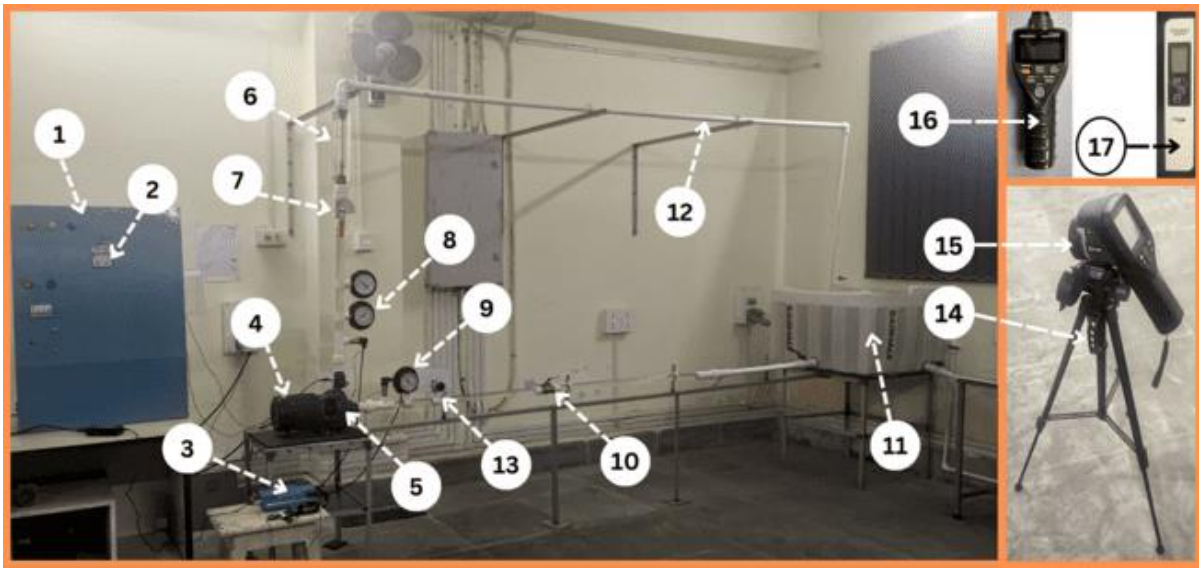

Fig. 2 Experimental Setup and Equipment

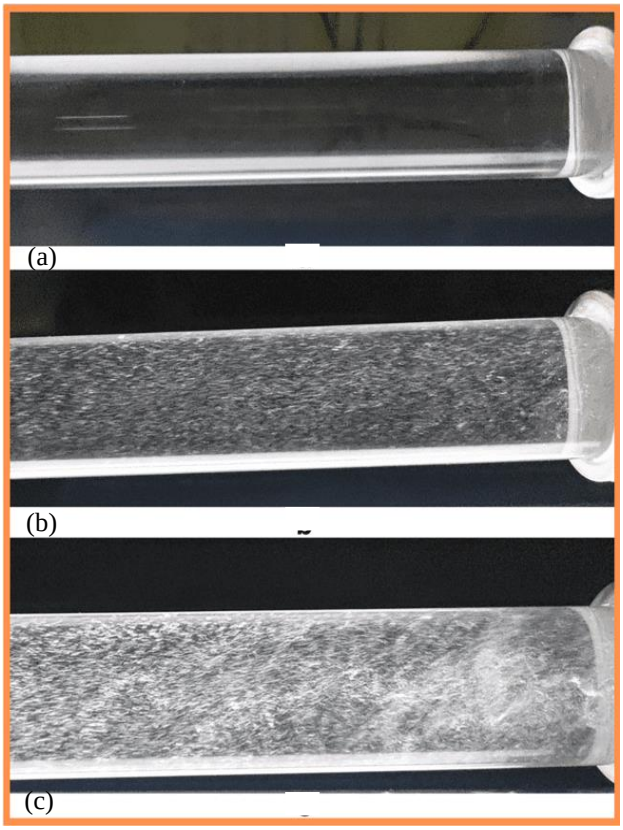

Fig. 3 Cavitation fault (a) Healthy (b) Low severity (c) High severity

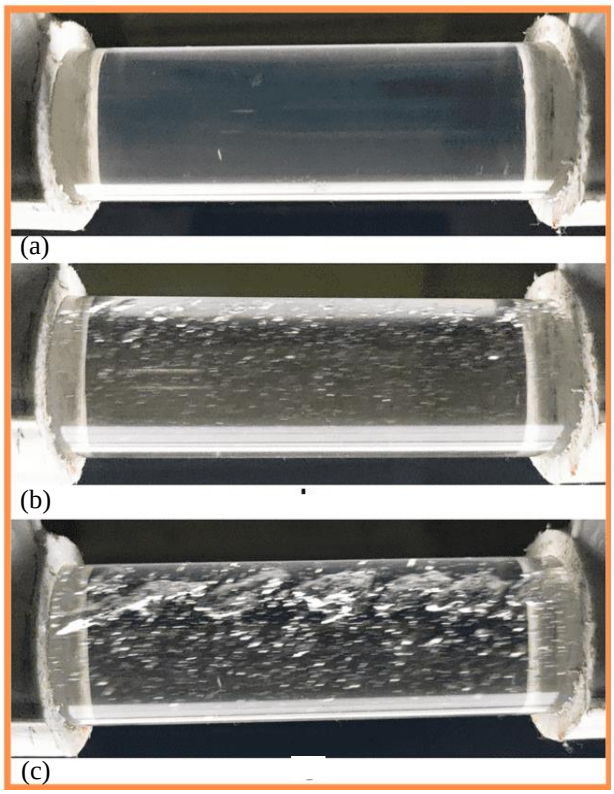

Fig. 4 Air Entrainment Fault (a) Healthy (b) Low severity (c) High severity

the inlet valve was progressively closed, the negative pressure on the inlet side increased, leading to the vaporization of water when it dropped below the liquid's vapor pressure. The formation and collapse of vapor bubbles in the pump impeller resulted in cavitation, which we closely monitored using infrared thermography. We observed that the severity of cavitation was directly related to the extent of valve closure, with increased valve closure leading to a higher occurrence of cavitation. The detected cavitation manifested in performance loss, characterized by head drop, and potential damage to the impeller blades which is evident by reduced inlet and outlet pressure which directly correlates to head drop and reduced flow rates for different speeds of centrifugal pump. The air entrainment fault was simulated by injecting air through an air injection valve which increased the inlet pressure of the system. The simulated faults can be seen at the inlet side through transparent pipes in Fig. 3 and Fig. 4.

The experimental technique began with the parameters of the thermal camera being configured conferring to the experimental environment, with the majority of these parameters being set automatically. However, as indicated in Table 3, such as emissivity, distance, ambient temperature, and relative humidity.

Table 3 Thermal camera description and fault types

Thermal camera (FLIR E60)	Lens: FOL 18 mm IR Sensor: 320 x 240 60 Hz (76,800-pixel resolution) Thermal sensitivity: < 0.05 °C Temperature range: -20 to 650 °C Minimum focus distance: 1.3 ft Accuracy: ± 2 °C. *Ambient Temperature:* 25 °C *Humidity:* 26 % *Emissivity* **ε**: 0.95
Fault Simulator	Healthy motor and pump Cavitation fault Air Entrainment fault

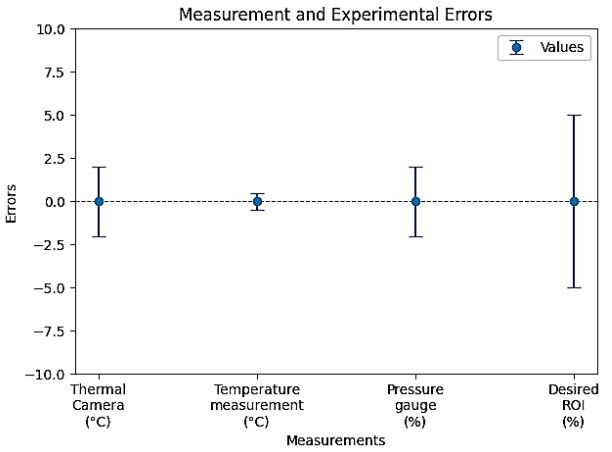

Fig. 5 Experimental and measurement errors

All parameters were set based on the test rig circumstances and were kept constant across all trials to ensure that all faults had the same dimension.

The study began with the capture of a thermal image of a healthy pump state, which was later used as a reference image to compare to the image of a faulty pump. The motor was set to normal operation with a full speed of 2700 RPM for the experiment. Thermal images were captured at an interval of 5 min for a total duration of 60 min for each fault level, to develop a trend in the temperature rise. The system was reset after each experiment for every fault level to have similar initial states of the system. Several experiments were performed and repeated to obtain an accurate estimate of the temperature changes.

To develop a trend on how each fault affects the temperature changes in the motor, separate experiments were performed. Experimental readings were taken at an interval of 1 hr for a total duration of 4 hrs, for each fault type. The fault severity level of the system was increased every hour to measure how substantial is the change. The severity levels were healthy, low and high, in respect of time. The description of the fault severity was measured in the form of inlet pressure changes ΔP_{inlet}. Experimental errors associated with equipment, measurements, and human errors are shown in Fig. 5.

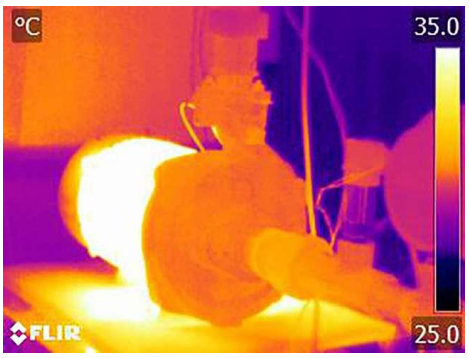

Fig. 6 Captured IRT Image

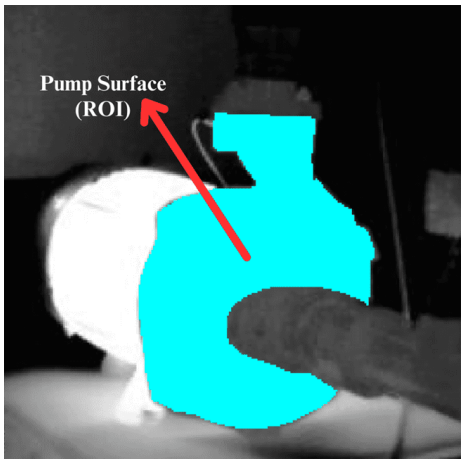

Fig. 7 Desired ROI in IRT Image

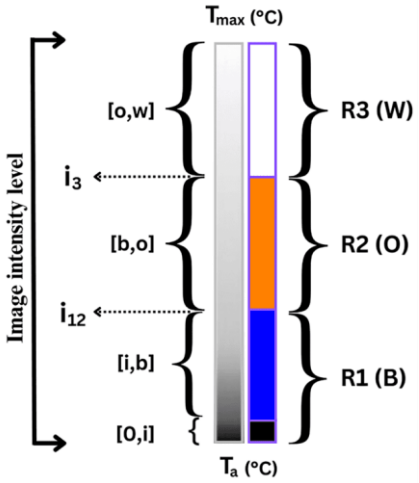

Fig. 8 Color Template

The next section discusses the proposed pseudo-coloring algorithm for fault severity analysis.

3. PROPOSED ALGORITHM FOR FAULT SEVERITY ESTIMATION USING PSEUDO COLORING

The captured thermal image R(r,c) and desired ROI (I_1(r,c)) are shown in Fig. 6 and Fig. 7 respectively. To analyze the severity of the fault a pseudo-coloring method was used after pre-processing of the original image. The temperature ranges for pseudo coloring are shown in the color template Fig. 8.

The temperature ranges for the template was identified by computing the greyscale histogram of the original image. Temperature range boundaries were decided based on the optimization of temperature range R_3 which contributed to the brightest or in terms of temperature the highest temperature zone.

The following steps have been followed for the optimization of thermal image temperature ranges:

Step 1: Capture RGB thermal image *R*(r,c) after a suitable time.

Step 2: Modify *R*(r,c) to I(r,c) by setting the lower temperature limit to T_a (ambient) and upper-temperature limit to T_{max} (maximum temperature reached in case of highest fault severity).

Step 3: Crop the desired ROI image I_1(r,c) from the *I*(r,c) image.

Step 4: Convert I_1(r,c) to greyscale image *G*(r,c).

Step 5: Compute values of "$i_3 = \mu + n\sigma$" for various values of *n*, where *(n = -3,-2,-1,0,1,2,3)*, the healthy state image is used as reference.

Step 6: For each value of i_3, compute W_{high} and W_{low}, where W_{high} and W_{low} are the numbers of pixels in the temperature range R_3 of high and low severity faults in greyscale images.

Step 7: Compute Optimization Delta Quotient *(ODQ)* values for each i_3 reference point using (9).

The different greyscale intensity charts for different thermal images obtained through various experiments showed, that a reference point could be made using the low-severity greyscale intensity distribution. The reference point was obtained through $i_3 = \mu + n\sigma$, where the optimized value of *n* was obtained through Optimization Delta Quotient *(ODQ)* performing various experiments. The point i_3 specified a reference point in the greyscale above which all pixels were counted towards severity. The important observation made through ODQ was that it will promote accuracy and early detection of a fault, as the ODQ gives the delta ratio of the number of pixels in R_3 temperature range for high vs low severity faults.

By comparing R_3 pixel values of high and low severity fault greyscale images, an *ODQ* was obtained which identifies the greyscale intensity value of i_3, which was best suited for severity analysis according to the relative change Eq. (9).

$$ODQ = \frac{W_{high} - W_{low}}{W_{low}} \tag{9}$$

Several experiments were performed to determine the optimized value of *n*. The best value of i_3 was obtained using the value of *n* which had the highest *ODQ* and the intensity value of temperature range R_3 was marked to be from i_3 to *1*. Intensity values for temperature range R_2 and R_1 in the template Fig. 8 were obtained by $i_{12} = \frac{1-(1-i_3)}{2}$, where R_1 lies from *0* to i_{12} and R_2 lies from i_{12} to i_3. The maximum temperature T_{max} was obtained by the experimental results, which occurred at the highest fault

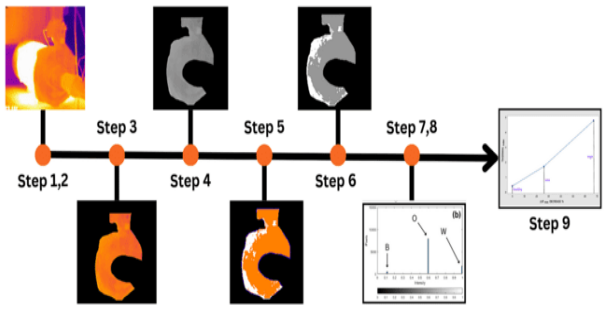

Fig. 9 Pseudo-coloring methodology

severity during the experiment and T_a being the ambient temperature.

The pseudo color template considered in this paper has three temperature ranges and as described above, temperature range R_3 is critical in terms of severity estimates, also this temperature range presence indicates an anomaly in the system which can be used as fault detection. To estimate the severity of the fault, $Thermal_{index}$ given in relative change Eq. (10) has been calculated between faulty (f) and healthy (h) states, by following the steps below also shown by Fig. 9:

Steps 1-4: Same Steps (1-4) are followed as given above for computing ODQ.

Step 5: Obtain pseudo color image (*P)* from *G*(r,c) according to the color template Fig. 8.

Step 6: Convert pseudo color image (*P*) to greyscale image *F*.

Step 7: Obtain histogram (greyscale intensity vs no. of pixels) of *F*.

Step 8: Compute the number of pixels of *B*, *O*, and *W* from the histogram of *F* for faulty *(f)* and healthy *(h)*.

Step 9: Calculate $Thermal_{index}$ using (11), which indicates the severity of the fault.

$$Thermal_{index} = \frac{(pixels*weightages)_{faulty} - (pixels*weightages)_{healthy}}{(pixels*weightages)_{healthy}} \tag{10}$$

$$Thermal_{index} = \frac{(B_f*x_1 + O_f*x_2 + W_f*x_3)_f - (B_h*x_1 + O_h*x_2 + W_h*x_3)_h}{(B_h*x_1 + O_h*x_2 + W_h*x_3)_h} \tag{11}$$

Where B, O, and W are the no. of pixels in specified ranges and x_1, x_2, and x_3 are the weights assigned to each temperature range.

B: Blue color, R_1, number of pixels present in the histogram of image *F* from intensity range (0 to i_{12}).

O: Orange color, R_2, number of pixels present in the histogram of image *F* from intensity range (i_{12} to i_3).

W: White color, R_3, number of pixels present in the histogram of image *F* from intensity range (i_3 to 1).

The assumptions considered for the implementation of this methodology were that the thermal images considered in *Step 1* were in the temperature range of T_a to T_{max} °*C*, the healthy state for high severity faults should have equal

or greater maximum temperature compared to the healthy state of the low severity faults and also the ODQ values were computed to be zero in the case where there are no pixels in R_3 temperature range of either low or high severity fault, which prevents selecting an i_3 value which is ineffective in early fault detection.

The weights assigned to the temperature ranges are obtained by considering the importance of all temperature ranges and expert opinion. R_3 being the critical temperature range was given the highest weightage (x_3) of 0.7 and temperature ranges R_2 and R_1 were given 0.2 and 0.1 weightages (x_2 and x_1) respectively. The next section discusses the proposed methodology for fault detection using image segmentation approach.

4. PROPOSED METHODOLOGY FOR FAULT DETECTION USING IMAGE SEGMENTATION

The detection of faults in pumps using image segmentation has been proposed in Fig. 10Fig. 9. This methodology involves separating the region of interest (ROI) from the original thermal image of the pump and converting it into an HSV color model image. The areas of thermal variation are then extracted from the image based on the Hue region. Fig. 24 illustrates the Hue region for healthy and faulty images with different faults.

Following that, edge detection is used based on the Hue image's threshold, and gradient-based edge detection algorithms such as Otsu, Roberts, Sobel, Canny, and Prewitt were used to detect the temperature fluctuations associated with various pump failures. The proposed methodology illustrates image segmentation tools' capacity to detect abnormalities in the Hue image.

After applying various segmentation techniques to all pump thermal images, the image matrices are calculated. These matrices include Mean, Kurtosis, Skewness, Contrast, Edge connectivity, PSNR,

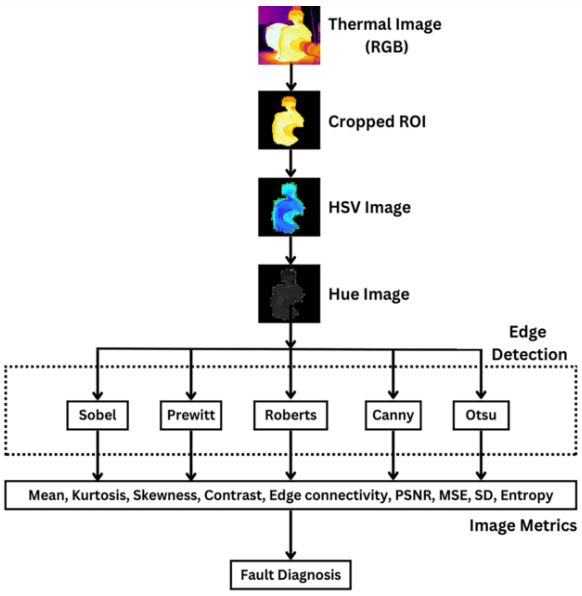

Fig. 10 Image segmentation methodology

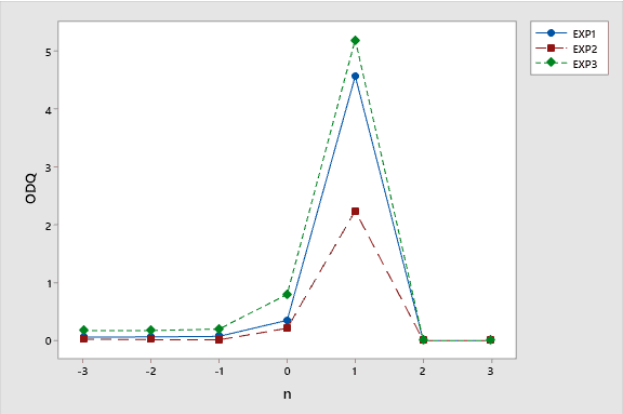

Fig. 11 ODQ vs n plot for various experiments

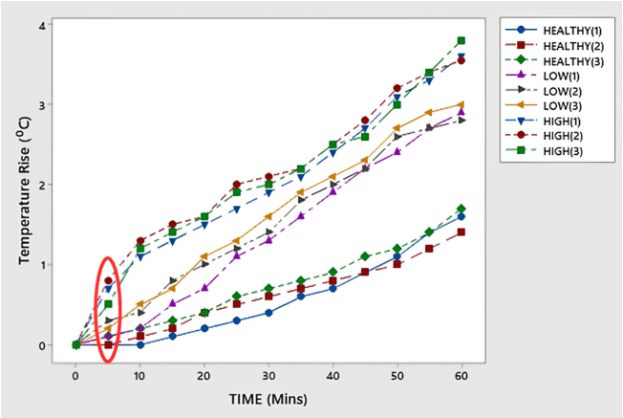

Fig. 12 Trend of rising pump temperature under cavitation phenomena for various experiments

MSE, SD, and Entropy. They are used to extract the best information from the image and to discriminate between the faults. The next section discusses the results obtained after the successful implementation of these methodologies onto the pre-processed thermal images.

5. RESULTS & DISCUSSION

5.1 Pseudo Coloring of Centrifugal Pump for Fault Severity Estimation

The severity of faults in centrifugal pumps was investigated by acquiring thermal images of healthy pumps and pumps exhibiting cavitation and air entrainment faults at varying severity levels. The methodology given in Section 3 was used to obtain the temperature ranges for pseudo coloring. Various experiments were performed to determine the optimal value of n which was essential to obtain the R_3 temperature range. As per Fig. 11, the highest ODQ values were found at an optimal value of n equal to 1.

To assess the thermal behavior of the pumps, a plot of temperature rise versus time was generated for each pump condition as demonstrated in Fig. 12 and Fig. . The results indicated that the temperature rise was significantly greater in pumps exhibiting cavitation and air entrainment faults when compared to healthy pumps. Furthermore, the magnitude of the temperature rise was positively correlated with the severity level of the faults.

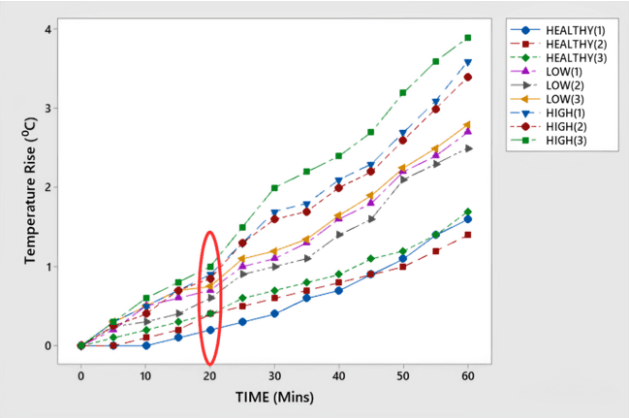

Fig. 13 Trend of rising pump temperature under air entrainment phenomena for various experiments

It was observed that the pump surface temperature increased gradually after the pump start-up and that the presence of cavitation and air entrainment faults was noticeable after 5 minutes of operation for both types of faults. However, the severity of the faults could be distinguished after 5 and 20 minutes of operation for cavitation and air entrainment faults, respectively.

For the purpose of enhancing the visualization of the thermal images, a pseudo-coloring technique was utilized to divide the grayscale images into distinct temperature ranges, in accordance with the guidelines outlined in color template Fig. 8. The pseudo-colored images for two healthy states, as well as low and high severity level faults, are presented in Fig. 14 and Fig. 16 for cavitation and air entrainment faults, respectively.

To make fair comparisons, Fig. 15 and Fig. 17 depict the corresponding grayscale images that were converted using the pseudo-colored images Fig. 14 and Fig. 16, while keeping the color intensities constant following the color template.

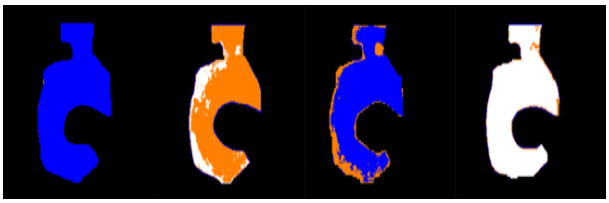

(a) (b) (c) (d)

Fig. 13 Pseudo color image (P) of (a) Healthy state 1 (b) Low severity fault (c) Healthy state 2 (d) High severity fault, under cavitation phenomenon

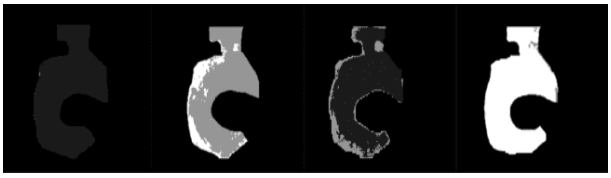

(a) (b) (c) (d)

Fig. 14 Greyscale image (F) of (a) Healthy state 1 (b) Low severity fault (c) Healthy state 2 (d) High severity fault, under cavitation phenomenon

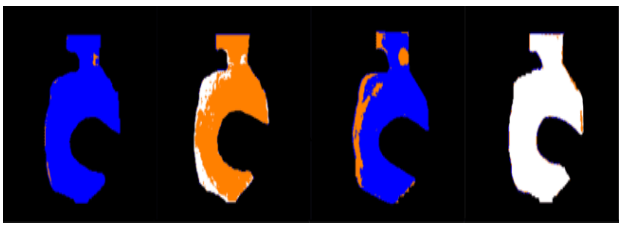

(a) (b) (c) (d)

Fig. 15 Pseudo color image (P) of (a) Healthy state 1 (b) Low severity fault (c) Healthy state 2 (d) High severity fault, under air entrainment phenomenon

(a) (b) (c) (d)

Fig. 16 Greyscale image (F) of (a) Healthy state 1 (b) Low severity fault (c) Healthy state 2 (d) High severity fault under, air entrainment phenomenon

The temperature distribution ranges were represented by the pseudo-colored images of cavitation and air entrainment faults in comparison to their respective healthy states. The images of the low-severity faults exhibited smaller R_3 temperature range, or white color, in comparison to the high-severity images, which showed a significant R_3 temperature range or white color. This demonstrated the effectiveness of the methodology in detecting the severity of faults in centrifugal pumps. In addition, the air entrainment high-severity fault image demonstrated a higher severity level than the cavitation image, as indicated by the R_3 temperature range for a similar pump run time. Furthermore, the methodology demonstrated flexibility, as it functioned perfectly well with different but similar temperature distributions of the pump's healthy state.

Histogram plots were generated for each image in Fig. 15 and Fig. 17 as presented in Fig. 18 and Fig. 19, with normalization to the grayscale. The findings indicated distinctive modifications in the distribution patterns of temperature intensities across different healthy and faulty pump conditions, at various severity levels.

The severity index for each pump condition was calculated to quantify the severity of the faults, following Eq. (11). This equation leverages the number of pixels present in all three intensity temperature ranges of the greyscale images of pseudo color images from the histogram. For both cavitation and air entrainment faults, $Thermal_{index}$ values were computed for each state of the pump, i.e., healthy, low severity fault, and high severity fault, as depicted in Fig. 20 and Fig. 21. The graphs demonstrate a significant upsurge in the $Thermal_{index}$ values as the severity of the fault increases, underscoring the efficacy of the current methodology.

The findings of this study demonstrate the effectiveness of thermal imaging in identifying and quantifying faults in centrifugal pumps. The temperature rise and pseudo-colored images provided clear indications

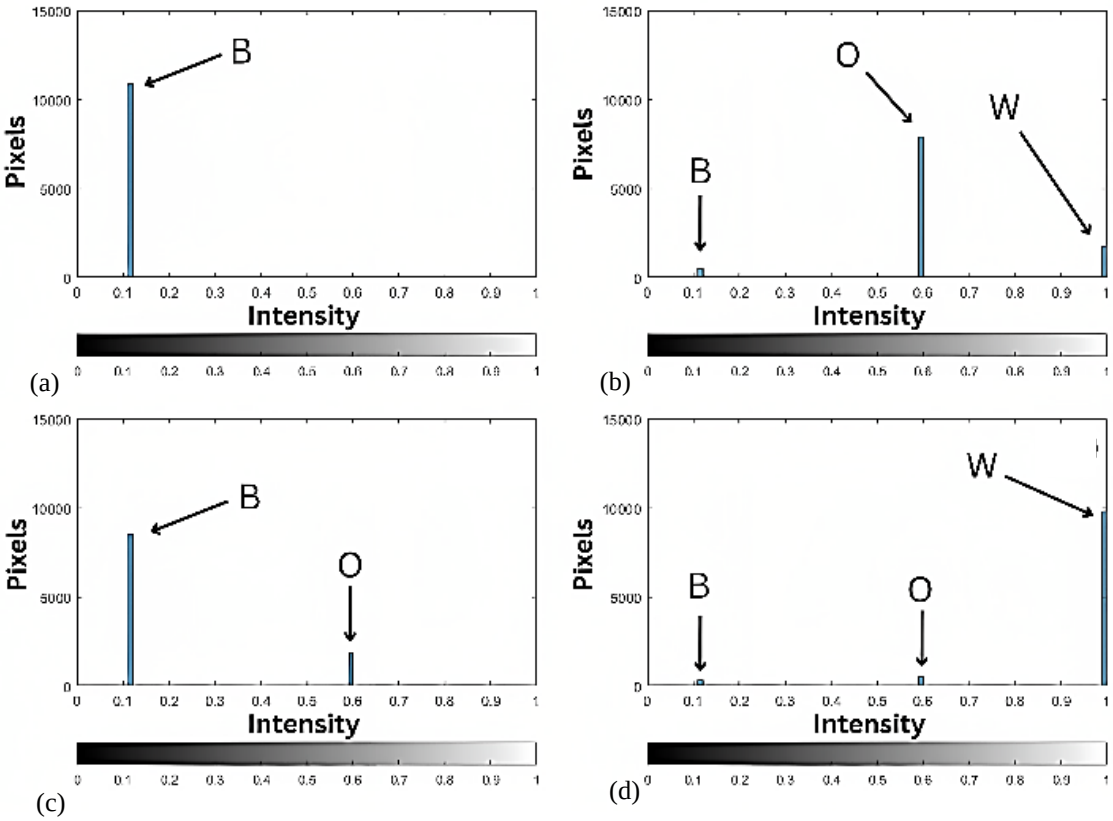

Fig. 17 Histogram of image (F) of (a) Healthy state 1 (b) Low severity fault (c) Healthy state 2 (d) High severity fault, under cavitation phenomenon

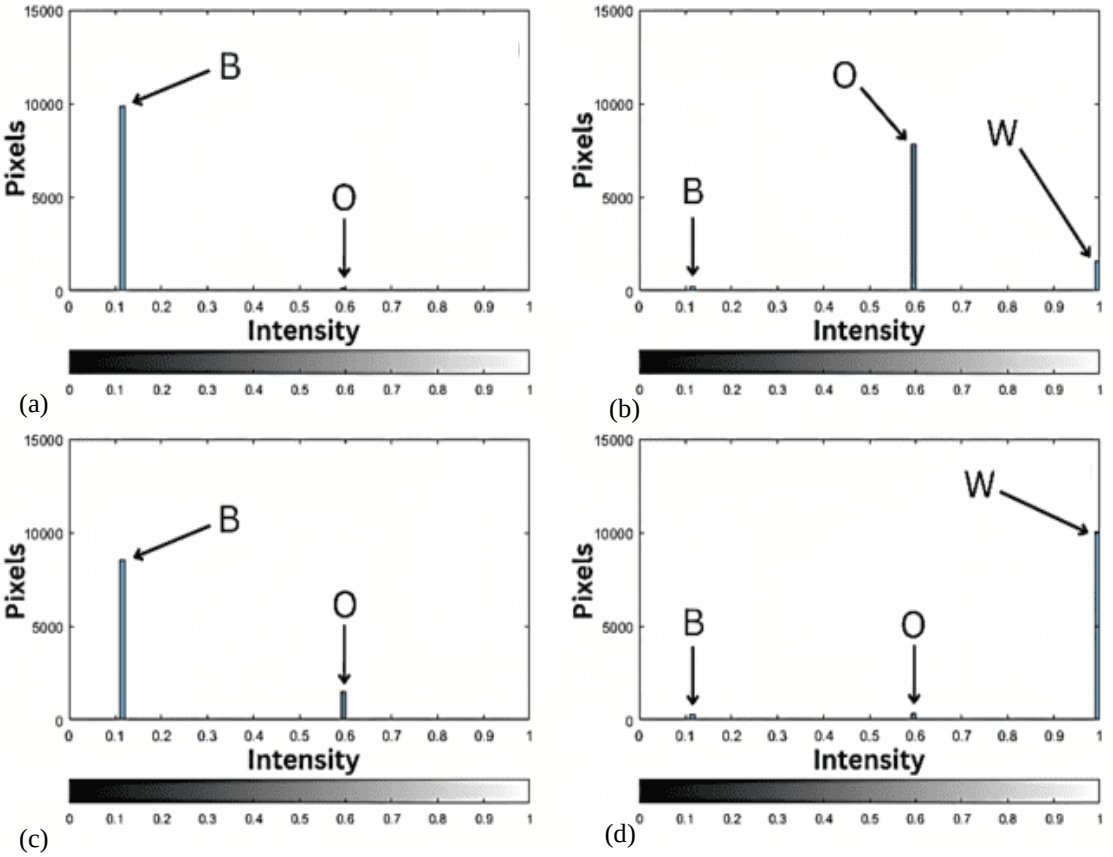

Fig. 18 Histogram of image (F) of (a) Healthy state 1 (b) Low severity fault (c) Healthy state 2 (d) High severity fault, under air entrainment phenomenon

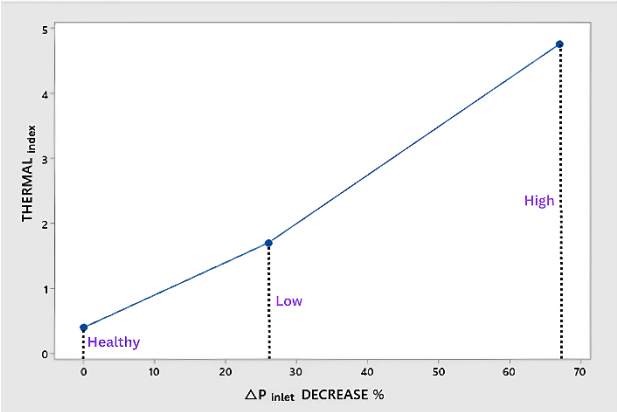

Fig. 19 Values of $Thermal_{index}$ under healthy and various levels of cavitation fault severity

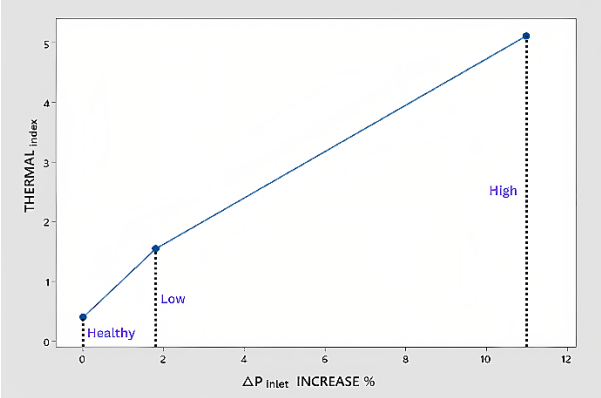

Fig. 20 Values of $Thermal_{index}$ under healthy and various levels of air entrainment fault severity

of the presence and severity of faults, which could assist in the early detection and diagnosis of potential pump failures.

5.2 Heat Dissipation pattern in centrifugal pump

When air or vapor enters the centrifugal pump chamber through, it significantly affects the heat dissipation process. Air is a poor conductor of heat compared to liquids, which are typically used as the working fluid in centrifugal pumps. Therefore, when air or vapor is present in the pump chamber, it acts as an insulating barrier and reduces the heat transfer rate between the pump components and the surrounding environment. This leads to an increase in the temperature of the pump components, which causes damage or failure of the pump.

Figure 22 illustrates the temperature distribution in a thermal image across the centrifugal pump at different temperature limits under faulty conditions after one hour of experimentation. The red color indicates the points that exceed the user-defined temperature limit. This visualization provides valuable insights into the propagation of heat dissipation and the locations with the maximum temperature gradient. The analysis reveals that the heat dissipation initially occurs near the eye of the impeller and throat region, which then spreads to other

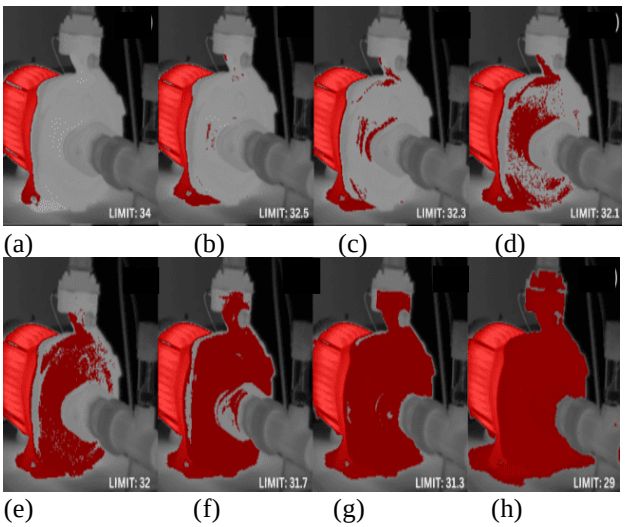

Fig. 21 Heat dissipation pattern in the thermal image, pixel values above (a) 34 °C (b) 32.5 °C (c) 32.3 °C (d) 32.1 °C (e) 32 °C (f) 31.7 °C (g) 31.3 °C (h) 29 °C

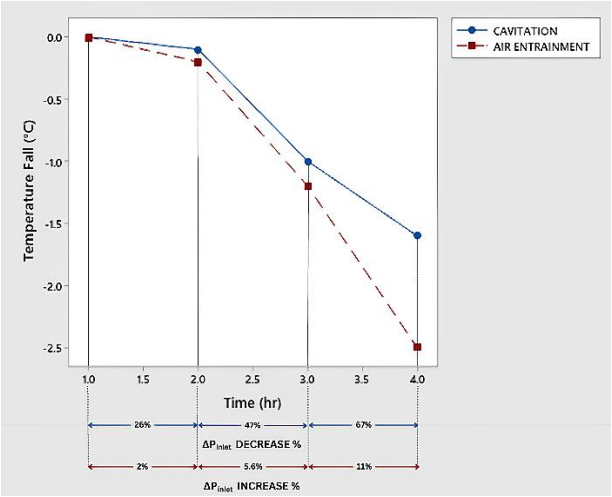

Fig. 22 Trend of falling motor temperature for varying cavitation and air entrainment fault severity

sections of the pump. Interestingly, similar effects were observed for both cavitation and air entrainment faults.

5.3 Motor Temperature Trend

The induction motor plays a crucial role in the operation of centrifugal pumps, and understanding the thermal effects of various pump faults on the motor is important. Surprisingly, the study revealed that as the severity of the pump fault increased, the temperature of the motor decreased, which is contrary to the trend observed in the pump temperature as demonstrated in Fig. 23. This unexpected phenomenon can be attributed to the fact that the motor load is reduced in proportion to the ratio of water to air when the working fluid is mixed with vapor or air.

The temperature delta in Celsius degrees relative to the healthy state is presented in Fig. 23. The motor's thermal data was collected during continuous pump operation for four hours, with increasing fault severity every hour for both types of faults, as depicted in Fig. 23.

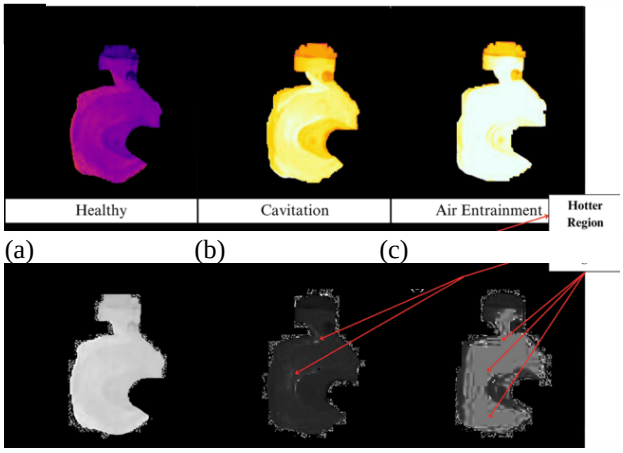

Fig. 23 RGB image (a) healthy (b) high severity cavitation (c) high severity air-entrainment (d,e,f) respective hue images

The results displayed also indicate that the temperature reduction in the motor is more prominent in cases of air entrainment fault compared to cavitation.

5.4 Edge Detection for Fault Detection

The hue region image in Fig. 24 exhibited clear areas of thermal variation, demonstrating the successful implementation of the proposed Hue image technique and image segmentation methods for detecting thermal variations without relying on the grayscale color model.

The presented study showcases the variations in image segmentation among distinct faults in centrifugal pumps. It is demonstrated that image segmentation techniques possess the capability to detect thermal variations by utilizing Hue images, after applying edge detection methods on the region images.

The hotter regions in cases of cavitation are concentrated around the eye of the impeller and throat, whereas in air entrainment phenomena, the hotter region is uniformly distributed as shown in Fig. 24. The outcomes of Fig. 25. reveal that distinct image segmentation approaches generate unique patterns for both faults, thus enabling the proposed technique to accurately detect pump faults. These findings demonstrate that each fault is characterized by its temperature pattern.

This observation implies that the proposed image segmentation method based on the Hue model is suitable to detect the temperature pattern and also recognize the precise fault based on the pump temperature signature. In contrast to grayscale image segmentation, which may lose a substantial portion of the image information during conversion, the proposed Hue image segmentation provides a superior approach for acquiring as much information as possible for accurate motor fault detection. Therefore, this paper utilizes the Hue image segmentation method to obtain precise information to improve the accuracy of pump fault detection.

Table 4, Table 5 and Table 6 present the image matrices for Mean, Kurtosis, Skewness, Contrast, Edge connectivity, PSNR, MSE, SD, and Entropy for each segmentation method. The results obtained from these

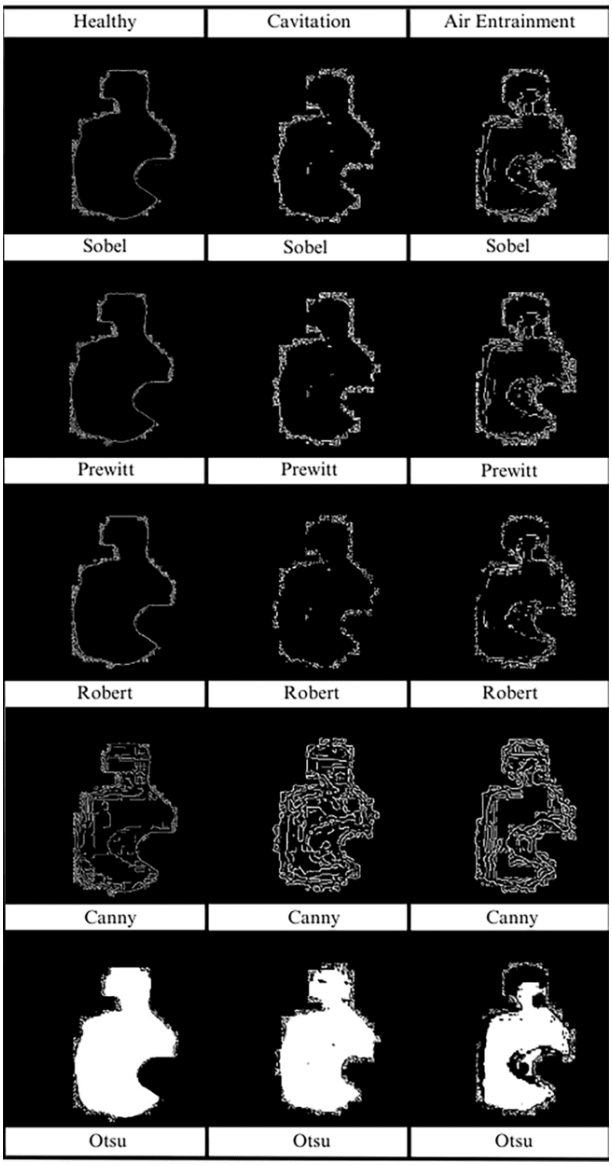

Fig. 24 Thermal image segmentation for healthy, cavitation, and air entrainment fault with different segmentation methods

tables indicate that image metric methods based on the Hue region exhibit discriminatory attributes for identifying pump faults.

The Otsu method exhibited the highest mean of 0.1667 for healthy pump conditions, making it distinguishable for pump fault detection compared to other methods such as Sobel, Prewitt, Roberts, and Canny. Similarly, for high cavitation and air entrainment faults, the Otsu method had the highest mean of 0.1730 and 0.1253, respectively. The satisfactory results obtained by the Otsu method for pump fault detection are demonstrated in Table 4, Table 5 and Table 6.

Among all approaches, the Otsu method produced the best Kurtosis values, obtaining the ideal kurtosis value of 3. The skewness values obtained for various pump conditions were indicative of the data's normalcy and predicted distribution. increased skewness values corresponded to increased data skewness, while skewness

Table 4 Image metric values for thermal image with different segmentation methods under healthy pump condition

Image Metrics / Method	S	P	R	C	O
Mean	0.017018	0.018073	0.014818	0.031068	0.166745
Kurtosis	56.77783	53.34982	65.50186	30.21983	4.197301
Skewness	7.468456	7.235317	8.031305	5.405537	1.7881
Contrast	-0.11688	-0.11563	-0.11866	-0.09073	0.164632
Edge Connectivity	273.375	296	237.375	1140.75	11789.88
PSNR	9.317907	9.303214	9.409476	9.835841	21.53683
SD	0.1293	0.133216	0.120824	0.1735	0.3728
MSE	0.117006	0.117403	0.114565	0.103852	0.00702
Entropy	0.1244	0.1305	0.1113	0.1997	0.6502
SD = Standard Deviation, PSNR = Peak to Signal Noise Ratio, MSE = Mean Square Error, O = Otsu, R = Roberts, S = Sobel, P = Prewitt, C = Canny.					

Table 5 Image metric values for thermal image with different segmentation methods under cavitation phenomenon

Image Metrics / Method	S	P	R	C	O
Mean	0.017018	0.019518	0.01099	0.041836	0.173073
Kurtosis	56.77783	49.25406	89.00637	21.94656	3.987208
Skewness	7.468456	6.946514	9.381171	4.576741	1.728354
Contrast	-0.0133	-0.01064	-0.01847	0.014193	0.172655
Edge Connectivity	366.25	421.375	117.625	1371.75	12016.13
PSNR	16.93113	16.51381	18.88813	14.1494	9.302604
SD	0.1293	0.138338	0.104254	0.2002	0.3783
MSE	0.020272	0.022316	0.012918	0.038464	0.117419
Entropy	0.1244	0.1387	0.0873	0.2506	0.6647
SD = Standard Deviation, PSNR = Peak to Signal Noise Ratio, MSE = Mean Square Error, O = Otsu, R = Roberts, S = Sobel, P = Prewitt, C = Canny.					

values for all pump conditions ranged from 1.7283 to 9.3811, indicating highly skewed data.

Generally, higher contrast levels in an image display a greater degree of grayscale variation. The Otsu method provided the highest values of contrast, namely 0.1646, 0.1726, and 0.1160 for healthy, cavitation, and air entrainment fault conditions, respectively.

The appropriate edge connectivity metric preferred value depends on the specific application. For more general patterns of temperature variation indicating broader faults such as wear or erosion, higher edge connectivity is more appropriate. For sharp, well-defined edges to detect localized faults such as cracks or fractures, a lower edge connectivity value is more appropriate. The Otsu method yielded the highest values of edge connectivity of 11789.88, 12016.13, and 7855.875 while Robert's method provided the lowest values of 237.376, 117.625, and 197.625 for different pump conditions.

The values of Mean Squared Error (MSE) and Peak Signal-to-Noise Ratio (PSNR), for which smaller MSE and higher PSNR are preferred, were used to evaluate the performance of the proposed method. The Otsu method yielded the highest average value of PSNR (21.53683) and the lowest MSE (0.00702) value for the healthy pump. Additionally, it obtained differentiated values of PSNR (9.302604 and 14.12941) and MSE (0.117419 and 0.038642) for different pump conditions. The maximum and minimum values of PSNR (14.49977 and 18.88813) and MSE (0.012918 and 0.035483) respectively, for cavitation and air-entrainment fault were obtained by Robert's method. These results demonstrate that the

Table 6 Image metric values for thermal image with different segmentation methods under air entrainment phenomenon

Image Metrics / Method	S	P	R	C	O
Mean	0.026367	0.027969	0.018945	0.04237	0.125378
Kurtosis	35.95301	33.78296	50.80282	21.64597	6.119257
Skewness	5.912107	5.725641	7.057111	4.543783	2.262577
Contrast	-0.03516	-0.03321	-0.04198	-0.01447	0.116082
Edge Connectivity	420.875	433.125	197.625	1398.5	7855.875
PSNR	13.64788	13.57388	14.49977	13.16668	14.12941
SD	0.1602	0.164884	0.136333	0.2014	0.3311
MSE	0.043173	0.043915	0.035483	0.048232	0.038642
Entropy	0.1758	0.1841	0.1355	0.2531	0.5446
SD = Standard Deviation, PSNR = Peak to Signal Noise Ratio, MSE = Mean Square Error, O = Otsu, R = Roberts, S = Sobel, P = Prewitt, C = Canny.					

proposed method extracted good features from the images compared to other methods.

Entropy can provide information about the distribution of temperature values in a thermal image. The Otsu method obtained the highest entropy values compared to other methods as 0.6502, 0.6647, and 0.5446.

The maximum values of standard deviation measures were obtained by the Otsu method as 0.3728, 0.3783, and 0.3311, which yielded nearly similar values and were less helpful in detecting pump faults, which may lead to misclassification of the faults.

In the analysis, it was observed that the extracted features proved useful for the detection and identification of pump faults. However, the ability to ascertain the severity of the fault was found to be lacking due to the overlapping of features, as noticed during the image processing of multiple thermal images displaying varying degrees of severity.

The results of the study demonstrate that image segmentation based on the Hue color model can effectively identify cavitation and air entrainment faults in centrifugal pumps. The proposed model is capable of extracting significant features for pump fault identification without requiring the use of any classifier. Additionally, image metrics played a crucial role in extracting essential information from the segmented Hue image, enabling accurate recognition of pump faults. The proposed segmentation methods and metrics were found to be highly effective in not only detecting the faults but also diagnosing them. However, the study highlighted some difficulties in distinguishing between the severity of faults, which were addressed earlier in the paper.

Overall, the Otsu method outperformed other methods in achieving satisfactory results and can be used for fault detection based on the proposed HSV color model. These results demonstrate the successful application of the proposed image segmentation methods in the identification and detection of faults in centrifugal pumps, and their potential for improving fault detection and identification in these machines. The next section will discuss the conclusions drawn from the above results.

6. CONCLUSION

The proposed methodology introduces a novel approach to the condition monitoring of centrifugal pumps. Only a limited number of existing literature sources are present which are dedicated to the exclusive examination of bearing faults in centrifugal pumps through the utilization of IRT. Through the continuous assessment of the health of centrifugal pumps and the identification of faults, our technique contributes to proactive maintenance, averting unforeseen breakdowns, reducing downtime, and optimizing pump operation. This is achieved by ensuring early detection and timely intervention, ultimately resulting in the enhancement of pump performance, operational efficiency, and the extension of equipment lifespan. To investigate the changes in the thermal signature of centrifugal pumps under cavitation and air entrainment faults, an experimental study was carried out to simulate different fault severities on a test rig. The analysis of these results produces the following key points:

1. The use of image processing techniques to analyze thermal images obtained from infrared thermography is effective in diagnosing faults related to cavitation and air entrainment in centrifugal pumps with an error of 1^{o}C.
2. The research work presents a new approach for condition monitoring and fault diagnosis of centrifugal pumps with a comprehensive methodology for fault detection and fault severity analysis.
3. The use of statistical measures and edge detection techniques is effective in achieving fault diagnosis and severity analysis in centrifugal pumps. Otsu is the

superior edge detection method with the highest mean of 0.1667, 0.1730, and 0.1253 for healthy, cavitation, and air-entrainment faults.

4. The temperature differential between the healthy and faulty state of the centrifugal pump surface increases as the fault severity increases.
5. The temperature differential for cavitation fault (1.65) was found to be higher than that for air entrainment fault (1.6) at low severity levels. However, for higher severity levels, the temperature differential was observed to be higher in air entrainment fault (5.12) than in cavitation fault (4.75), as evidenced by the $Thermal_{index}$ values.
6. It was observed that the pump surface temperature increased gradually after the pump start-up and that the presence of cavitation and air entrainment faults were noticeable after 5 mins of operation for both types of faults. However, the severity of the faults could be distinguished after 5 and 20 mins of operation for cavitation and air entrainment faults, respectively.
7. The heat dissipation pattern in the thermal image of a centrifugal pump on different temperature limits suggested a higher temperature gradient near the eye of the impeller and throat regions of the centrifugal pump.
8. An intriguing observation was made during the experimental investigation of centrifugal pumps, wherein a phenomenon was noted. It was observed that as the severity of the fault increased, there was a decline in the temperature differential of the driver motor. This phenomenon can be attributed to the decrease in motor load caused by the presence of an air-water mixture within the pump chamber. The effects of this phenomenon were also apparent in the RPM and Current (A) of the motor. Notably, the fault associated with air entrainment exhibited a more pronounced reduction in load compared to the fault associated with cavitation.

Certain limitations associated with the utilization of IRT as a fault diagnosis tool for centrifugal pumps have been identified. These encompass restricted fault differentiation, challenges pertaining to real-time monitoring, and the need for seamless integration with maintenance strategies. In conclusion, our study demonstrates the effectiveness of infrared thermography for diagnosing cavitation and air entrainment faults in centrifugal pumps, promoting proactive maintenance and enhanced performance. While this research sheds light on improved monitoring, it also reveals challenges in fault differentiation and real-time tracking. Further studies are crucial to unlock the full potential of infrared thermography in diagnosing various centrifugal pump faults.

ACKNOWLEDGEMENTS

The authors would like to thank the Subir Chowdhury School of Quality and Reliability for their support in the experimental assessment at the Indian Institute of Technology Kharagpur.

CONFLICT OF INTEREST

The authors have no conflict of interest to disclose in this research work.

AUTHORS CONTRIBUTION

A. K. Goel: Conceptualization, Data Collection, Methodology, Investigation, Validation, Writing original draft and editing; **V. N. A. Naikan**: Supervision, Validation, Review.

REFERENCES

Alfayez, L., Mba, D., & Dyson, G. (2005). The application of acoustic emission for detecting incipient cavitation and the best efficiency point of a 60 kW centrifugal pump: Case study. *NDT and E International*, *38*(5), 354–358. https://doi.org/10.1016/j.ndteint.2004.10.002

Al-Musawi, A. K., Anayi, F., & Packianather, M. (2020). Three-phase induction motor fault detection based on thermal image segmentation. *Infrared Physics and Technology*, *104*. https://doi.org/10.1016/j.infrared.2019.103140

Al-Obaidi, A. R. (2019). *Numerical investigation of flow field behaviour and pressure fluctuations within an axial flow pump under transient flow pattern based on CFD analysis method.* Journal of Physics: Conference Series IOP Publishing. https://doi.org/10.1088/1742-6596/1279/1/012069

Al-Obaidi, A. R. (2020a). Experimental comparative investigations to evaluate cavitation conditions within a centrifugal pump based on vibration and acoustic analyses techniques. *Archives of Acoustics*, *45*(3), 541–556. https://doi.org/10.24425/aoa.2020.134070

Al-Obaidi, A. R. (2020b). Experimental investigation of cavitation characteristics within a centrifugal pump based on acoustic analysis technique. *International Journal of Fluid Mechanics Research*, *47*, 6. www.begellhouse.com

Al-Obaidi, A. R. (2020c). Influence of guide vanes on the flow fields and performance of axial pump under unsteady flow conditions: Numerical study. *Journal of Mechanical Engineering and Sciences*, *14*(2), 6570–6593. https://doi.org/10.15282/JMES.14.2.2020.04.0516

Al-Obaidi, A. R. (2021). Analysis of the effect of various impeller blade angles on characteristic of the axial pump with pressure fluctuations based on time- and frequency-domain investigations. *Iranian Journal of Science and Technology - Transactions of Mechanical Engineering*, *45*(2), 441–459. https://doi.org/10.1007/s40997-020-00392-3

Al-Obaidi, A. R., & Mishra, R. (2020). Experimental investigation of the effect of air injection on

performance and detection of cavitation in the centrifugal pump based on vibration technique. *Arabian Journal for Science and Engineering*, *45*(7), 5657–5671. https://doi.org/10.1007/s13369-020-04509-3

Al-Obaidi, A. R., & Mohammed, A. A. (2019). Numerical investigations of transient flow characteristic in axial flow pump and pressure fluctuation analysis based on the CFD technique. *Journal of Engineering Science and Technology Review*, *12*(6), 70–79. https://doi.org/10.25103/jestr.126.09

Al-Obaidi, A. R., & Towsyfyan, H. (2019). An experimental study on vibration signatures for detecting incipient cavitation in centrifugal pumps based on envelope spectrum analysis. *Journal of Applied Fluid Mechanics*, *12*(6), 2057–2067. https://doi.org/10.29252/jafm.12.06.29901

Chudina, M. (2003). Noise as an indicator of cavitation in a centrifugal pump. *Acoustical Physics*, *49*(4), 463–474. https://doi.org/10.1134/1.1591303

Čudina, M. (2003). Detection of cavitation phenomenon in a centrifugal pump using audible sound. *Mechanical Systems and Signal Processing*, *17*(6), 1335–1347. https://doi.org/10.1006/mssp.2002.1514

Glowacz, A., & Glowacz, Z. (2017). Diagnosis of the three-phase induction motor using thermal imaging. *Infrared Physics & Technology*, *81*, 7–16. https://doi.org/10.1016/j.infrared.2016.12.003

Glowacz, A., Glowacz, A., & Glowacz, Z. (2015). Recognition of thermal images of direct current motor with application of area perimeter vector and bayes classifier. *Measurement Science Review*, *15*(3), 119–126. https://doi.org/10.1515/msr-2015-0018

Goel, A. K., Singh, G., & Naikan, V. N. A. (2022). A methodology for selection of condition monitoring techniques for rotating machinery. *International Journal of Prognostics and Health Management*, *13*(2). https://doi.org/10.36001/ijphm.2022.v13i2.3205

Hidayat, A. Y., Widodo, A., & Dwi Haryadi, G. (2018). *Fault diagnostic system bearing centrifugal pump using k-means method for thermography image and signal analysis vibrations.* MATEC Web of Conferences, 159. https://doi.org/10.1051/matecconf/201815902006

Hosien, M. A., & Selim, S. M. (2017). Experimental and theoretical investigation on the effect of pumped water temperature on cavitation breakdown in centrifugal pumps. *Journal of Applied Fluid Mechanics*, *10*(4), 1079–1089. https://doi.org/10.18869/acadpub.jafm.73.241.27589

Kan, K., Binama, M., Chen, H., Zheng, Y., Zhou, D., Su, W., & Muhirwa, A. (2022). Pump as turbine cavitation performance for both conventional and reverse operating modes: A review. *Renewable and Sustainable Energy Reviews*, *168*. https://doi.org/10.1016/j.rser.2022.112786

Kazi, S. N., Al-Arabi, A. A. B., Selim, S. M. A., Saidur, R., & Duffy, G. G. (2011). Detection of Cavitation in Centrifugal Pumps. *Australian Journal of Basic and Applied Sciences*, *5*(10), 1260–1267. https://www.researchgate.net/publication/301779551

Liao, M., Si, Q., Fan, M., Wang, P., Liu, Z., Yuan, S., Cui, Q., & Bois, G. (2021). *Experimental study on flow behavior of unshrouded impeller centrifugal pumps under inlet air entrainment condition.* 14th European Conference on Turbomachinery Fluid Dynamics and Thermodynamics, ETC 2021. https://doi.org/10.3390/ijtpp6030031

McKee, K. K., Forbes, G. L., Mazhar, I., Entwistle, R., & Howard, I. (2014). *A review of machinery diagnostics and prognostics implemented on a centrifugal pump.* Lecture Notes in Mechanical Engineering. Springer Heidelberg. https://doi.org/10.1007/978-1-4471-4993-4_52

Mckee, K. K., Forbes, G., Mazhar, I., Entwistle, R., & Howard, I. (2011). *A review of major centrifugal pump failure modes with application to the water supply and sewerage industries*.

Muhirwa, A., Bisengimana, E., Binama, M., & Muhirwa, A. (2016). *Cavitation effects in centrifugal Pumps-A review.* Journal of Engineering Research and Applications www.ijera.com (Vol. 6). www.ijera.com

Paripurna Kamiel, B. (2015). *Department of Mechanical Engineering Vibration-Based Multi-Fault Diagnosis for Centrifugal Pumps Declaration*.

Samanipour, P., Poshtan, J., & Sadeghi, H. (2017). Cavitation detection in centrifugal pumps using pressure time-domain features. *Turkish Journal of Electrical Engineering and Computer Sciences*, *25*(5), 4287–4298. https://doi.org/10.3906/elk-1701-2

Sanchez, W., Carvajal, C., Poalacin, J., & Salazar, E. (2018). *Detection of cavitation in centrifugal pump for vibration analysis.* 2018 4th International Conference on Control, Automation and Robotics (ICCAR). https://doi.org/10.1109/ICCAR.2018.8384720

Schäfer, T., Neumann, M., Bieberle, A., & Hampel, U. (2017). Experimental investigations on a common centrifugal pump operating under gas entrainment conditions. *Nuclear Engineering and Design*, *316*, 1–8. https://doi.org/10.1016/j.nucengdes.2017.02.035

Singh, G., Anil Kumar, T. C., & Naikan, V. N. A. (2016a). *Fault diagnosis of induction motor cooling system using infrared thermography.* 2016 IEEE 6th International Conference on Power Systems (ICPS). https://doi.org/10.1109/ICPES.2016.7584040

Singh, G., Anil Kumar, T. C., & Naikan, V. N. A. (2016b). Induction motor inter turn fault detection using infrared thermographic analysis. *Infrared Physics and Technology*, *77*, 277–282. https://doi.org/10.1016/j.infrared.2016.06.010

Sojoudi, A., Nourbakhsh, A., & Shokouhmand, H. (2018). Experimental evaluation of temperature rise in centrifugal pumps at partial flow rates. *Journal of the*

Brazilian Society of Mechanical Sciences and Engineering, *40*, 1-11. https://doi.org/10.1007/s40430-018-1078-8

Soni, S. (2017). Increase productivity of centrifugal pump by detection of cavitation phenomena. *Indian Journal Of Applied Research*. https://doi.org/10.36106/ijar

Stan, M., Pana, I., Minescu, M., Ichim, A., & Teodoriu, C. (2018). Centrifugal pump monitoring and determination of pump characteristic curves using experimental and analytical solutions. *Processes*, *6*(2). https://doi.org/10.3390/PR6020018

Stopa, M. M., Cardoso Filho, B. J., & Martinez, C. B. (2014). Incipient detection of cavitation phenomenon in centrifugal pumps. *IEEE Transactions on Industry Applications*, *50*(1), 120–126. https://doi.org/10.1109/TIA.2013.2267709

Thobiani, A., & Al Thobiani, F. W. (2011). The Non-intrusive detection of incipient cavitation in centrifugal pumps. [Doctoral thesis, University of Huddersfield]. The Non-intrusive Detection of Incipient Cavitation in Centrifugal Pumps. By: Faisal Al Thobiani. In *By: Faisal Al Thobiani*.

Towsyfyan, H., Gu, F., Ball, A. D., & Liang, B. (2018). Modelling acoustic emissions generated by tribological behaviour of mechanical seals for condition monitoring and fault detection. *Tribology International*, *125*, 46–58. https://doi.org/10.1016/j.triboint.2018.04.021

Yan, Z., Liu, J., Chen, B., Cheng, X., & Yang, J. (2015). Fluid cavitation detection method with phase demodulation of ultrasonic signal. *Applied Acoustics*, *87*, 198–204. https://doi.org/10.1016/j.apacoust.2014.07.007